Revealing the nano-scale mechanisms of the limited non-basal plasticity in magnesium

Sang Ho Oh, Jiwon Jeong, Zhuocheng Xie, Markus Alfreider, Sandra Korte-Kerzel, Daniel Kiener, Julien Guénolé

Revealing the nano-scale mechanisms of the limited non-basal plasticity in magnesium

Jiwon Jeong[1,†], Zhuocheng Xie[2,†], Markus Alfreider[3], Sandra Korte-Kerzel[2], Daniel Kiener[3], Julien Guénolé[4,*], Sang Ho Oh[5*]

[1] Department of Structure and Nano-/Micromechanics of Materials, Max-Planck Institut für Eisenforschung GmbH, Düsseldorf, 40237, Germany
[2] Institute of Physical Metallurgy and Materials Physics, RWTH Aachen University, 52056 Aachen, Germany
[3] Department of Materials Science, Montanuniversität Leoben, Jahnstraße 12, 8700 Leoben, Austria
[4] Université de Lorraine, CNRS, Arts et Métiers ParisTech, LEM3, Metz, 57070, France
[5] Department of Energy Engineering, KENTECH Institute for Energy Materials and Devices, Korea Institute of Energy Technology (KENTECH), Naju 58330, Republic of Korea.

[†]These authors contributed equally
*Corresponding authors: shoh@kentech.ac.kr, julien.guenole@cnrs.fr

Abstract

$\langle c+a \rangle$ dislocations are considered as the primary defects limiting the ductility of magnesium. It is argued that in small magnesium crystals the glide of such dislocations can be activated to accommodate plastic strain at high flow stress levels that are rarely achieved in the bulk. Here, we report $\langle c+a \rangle$ dislocation-mediated small-scale plasticity of *c*-axis oriented submicrometer-sized magnesium pillars observed by *in situ* transmission electron microscopy compression tests. After mobile $\langle c+a \rangle$ dislocations accommodate the initial plasticity of pillars, interactions between dislocations develop local dislocation entanglements, thereby preventing consecutive dislocation glide and surface annihilation. Supported by atomistic simulations, this increased pinning and multiplication is attributed to the formation of basal I_1 and I_2 stacking faults, induced by interaction of glissile pyramidal II dislocations, which serve as anchor points for dislocation sources. The ensuing plastic strain is accommodated via dislocation avalanches caused by simultaneous activation of multiple dislocation sources at increasing stress levels, forming a dislocation forest of $\langle c+a \rangle$ dislocations in the confined volume. This observation distinctly differs to common small-scale plasticity associated with a dislocation starved or exhausted state and provides a new concept towards plasticity and work hardening in bulk Mg.

Keywords: Magnesium; small-scale plasticity; *in situ* compression; atomistic simulations

1 Introduction

Magnesium (Mg) alloys are attractive for automotive and aerospace applications due to their low density and ease of recycling[1–3]. However, Mg exhibits low ductility at room temperature, making processing and forming demanding and costly, thereby preventing widespread applications of wrought alloys. The poor intrinsic ductility of Mg is associated with the limited plastic deformability in the *c*-axis direction of the hexagonal close-packed (HCP) crystal structure, which is mediated primarily by the glide of pyramidal $\langle c+a \rangle$ dislocations[4]. Pyramidal $\langle c+a \rangle$ dislocations are reported to be intrinsically unstable, transforming to basal-dissociated sessile dislocation structures that cannot contribute to *c*-axis straining and serve as strong obstacles to the motion of other dislocations with a $\langle c \rangle$ component[5–8]. The resulting insufficient number of independent slip systems of Mg are unable to satisfy the von Mises criterium[9], causing anisotropic plastic deformation. To overcome this limitation, different material design strategies aiming at increasing non-basal dislocation sources[10–12], preventing $\langle c+a \rangle$ pyramidal-

to-basal transitions[6–8], or accelerating cross-slip of pyramidal $\langle c+a \rangle$ dislocations[13–15] were proposed for improving the ductility of Mg.

Recent work[16] reported notable dislocation mediated plasticity of sub-micrometer-sized Mg single crystals under *c*-axis compression by profuse glissile $\langle c+a \rangle$ dislocations on pyramidal planes. Pyramidal slip is activated in the submicron pillars due to mechanical size effects, namely by high flow stress levels allowing abundant activation of surface sources for $\langle c+a \rangle$ dislocations. Cross-slip of $\langle c+a \rangle$ dislocations between pyramidal planes has also been observed, resulting in the formation of sessile dislocation dipoles and debris lying along the pyramidal-basal intersection. However, how the small-scale plasticity of Mg is accommodated at a large strain remains unclear, considering that the small size relieves the difficulty of activating pyramidal slip but the resulting $\langle c+a \rangle$ dislocation glide, cross-slip and interaction are prone to form sessile dislocation products during the plastic flow. Additionally, the prevalent slip plane of pyramidal $\langle c+a \rangle$ dislocations is still under debate[17–22].

Here, we demonstrate the activation of profound pyramidal II $\langle c+a \rangle$ dislocations and the pronounced strain hardening associated with $\langle c+a \rangle$ dislocation interactions causing the formation of basal stacking faults via *in situ* transmission electron microscopy (TEM) compression testing of *c*-axis oriented single crystalline Mg nanopillars in conjunction with atomistic simulations. Furthermore, we reveal the atomistic mechanisms of the interactions of glissile pyramidal II $\langle c+a \rangle$ dislocations and the basal I_1 and I_2 stacking fault formation via molecular dynamics (MD) simulations.

2 Results

2.1 Orientation-dependent deformation behavior

To examine the details of pyramidal slip and its size-dependency, the *c*-axis oriented Mg pillars with different sizes were tested by *in situ* micro-compression in SEM. In this pillar orientation the $(2\bar{1}\bar{1}2)$ slip plane has a nominal Schmid factor of 0.45 for $\langle c+a \rangle$ dislocations, favoring pyramidal II slip (Table S1). For comparison, the $[2\bar{1}\bar{1}2]$ oriented pillars in the same size range were also tested to facilitate basal slip primarily by $\langle a \rangle$ dislocations. In the $[2\bar{1}\bar{1}2]$ oriented pillars the Schmid factors for basal and pyramidal II slip are 0.50 and 0.30, respectively. Figures 1a and b show the slip geometry as well as exemplary *in situ* TEM compression samples before and after the deformation of the *c*-axis and the $[2\bar{1}\bar{1}2]$ oriented pillars, respectively. Evidently, while the *c*-axis pillar exhibits a pronounced accumulation of dislocations in the plastically deformed volume (Fig. 1a), the $[2\bar{1}\bar{1}2]$ pillar deforms by formation of a strongly localized slip band (Fig. 1b), a well-known phenomenon for face-centered cubic (FCC) single crystals[23]. This difference in deformation behavior is observed over the whole range of considered sizes, with the *c*-axis pillars exhibiting rather smooth flow curves with minor load drops (Fig. 1c), while the $[2\bar{1}\bar{1}2]$ pillars tend to display discrete strain bursts (Fig. 1d). Unlike the localization and easy glide of $\langle a \rangle$ dislocations for basal slip, pyramidal slip by $\langle c+a \rangle$ dislocations resulted in more uniform deformation over a wide strain range (Fig. S1), but at a much higher stress level, which is consistent with previous reports (Movie S1)[24].

It is well known that the stochastic nature of plasticity is intimately linked to the dislocation content of the probed volume. The pillars prepared for *in situ* TEM compression are not completely free of dislocations, but contain some immobile dislocations that have not been removed upon annealing (Fig. S2, S3). Most pre-existing dislocations in the *c*-axis pillars exhibited a characteristic configuration: a short and inclined segment connected to a long

straight segment lying parallel to the pyramidal-basal intersection (Fig. S3). We performed **g·b** analyses to determine the Burgers vector of the dislocations. Except for a few dislocations which have only an $\langle a \rangle$ component, most dislocations have Burgers vector with both $\langle c \rangle$ and $\langle a \rangle$ components, and hence are $\langle c+a \rangle$ dislocations. Figure 1e shows that the dislocation density in the $[2\bar{1}\bar{1}2]$ pillar increases only slightly from the initial low value of ~10^{13} m^{-2} and never exceeds $2 \cdot 10^{13}$ m^{-2}. In contrast, the dislocation density in the *c*-axis pillar swiftly increases from initial ~10^{13} m^{-2} to ~$5 \cdot 10^{13}$ m^{-2} at a stable flow regime. This significant difference in dislocation accumulation between the two examined crystal orientations is also evidenced in the strength scaling behavior in Fig. 1f, where the basal slip orientation follows the common scaling exponent of 0.6, typical for crystals with low lattice friction and low dislocation density, where dislocations have high mobility. In the case of pyramidal slip, however, we find a reduced scaling exponent of 0.27, as encountered for pre-strained systems of mobile dislocation content or materials with a generally higher lattice friction and resulting low dislocation mobility[25,26].

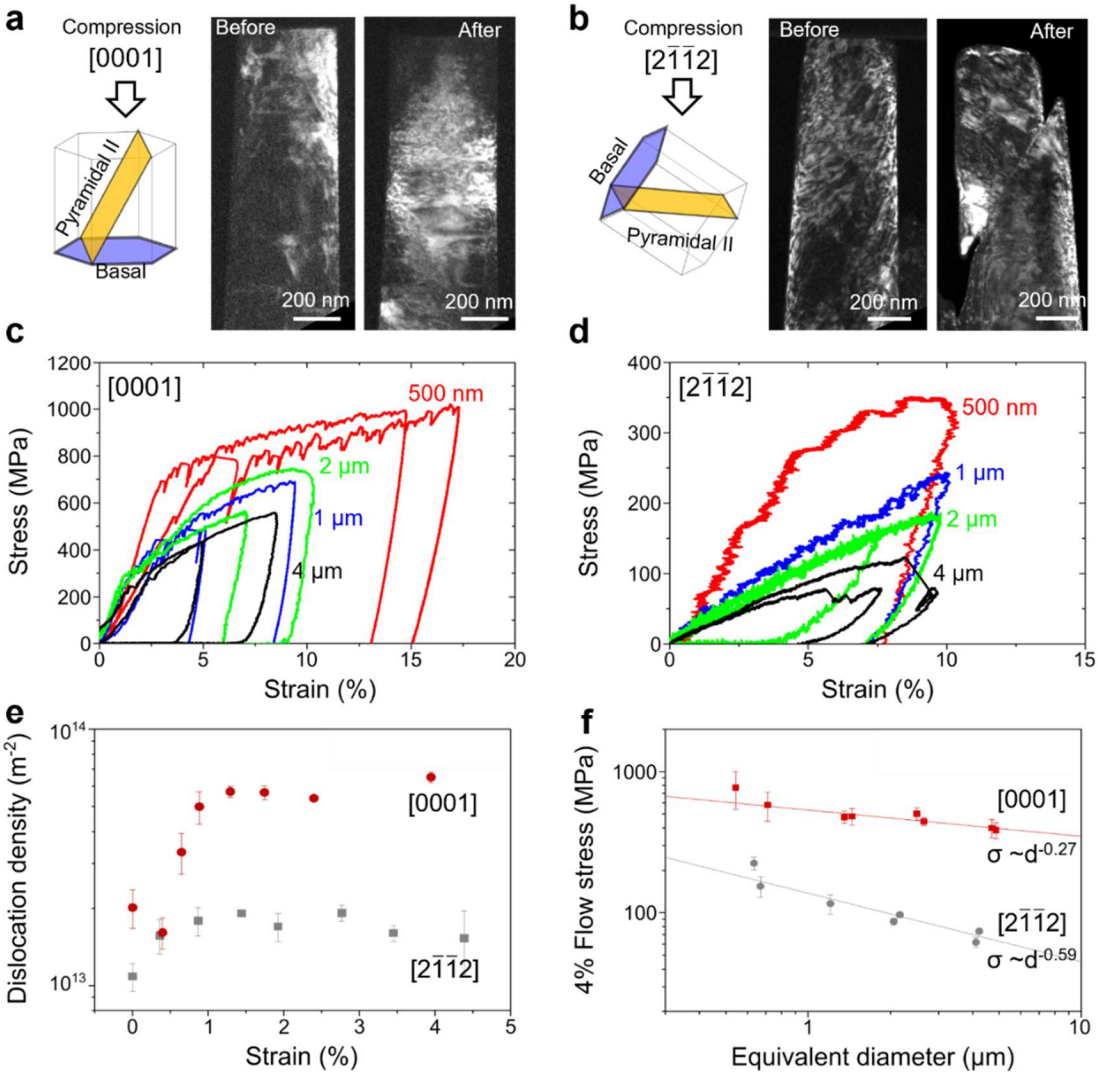

Fig. 1. Orientation-dependent deformation behavior of magnesium pillars. Pyramidal II and basal slip geometry and microstructure of Mg pillar before and after *in-situ* TEM compression test of (a) *c*-axis and (b) [2$\bar{1}\bar{1}$2]-oriented pillars. The primary deformation mode is pyramidal slip by <c+a> dislocations in the *c*-axis pillars and basal slip by <a> dislocations in the [2$\bar{1}\bar{1}$2] pillars, respectively. Stress-strain curves of (c) *c*-axis and (d)

[$2\bar{1}\bar{1}2$] pillars for different sizes (0.5-4 μm) displaying notably different mechanical responses. (e) Dislocation density evolution in the Mg pillars during *in-situ* TEM compression. An abrupt increase in dislocation density is observed in the *c*-axis pillar, while it remains approximately constant in the [$2\bar{1}\bar{1}2$] pillar due to the different deformation mechanisms. (f) 4% flow stress as a function of equivalent sample diameter showing the effect of crystal size and orientation effects for *c*-axis and [$2\bar{1}\bar{1}2$] pillars.

2.2 Onset of plasticity

All the *c*-axis pillars deformed uniformly with exhibiting large plastic strain without failure (Movie 2). *In situ* TEM observations reveal distinctive dislocation mediated slip processes. Figure 2 presents a brief overview of the evolution of the dislocation structure with strain. The initial plastic deformation of the pillar is carried by the nucleation and glide of $\langle c+a \rangle$ dislocations from the side surface near the top region of the pillar (orange arrow in Fig. 2a(ii)). These $\langle c+a \rangle$ dislocations with half-loop shape glide swiftly along a pyramidal plane to the other side surface with trailing a straight dislocation segment parallel to the pyramidal-basal intersection (blue arrow). With further straining, discrete pyramidal slip systems are activated intermittently, which also involve the formation of straight segments (Fig. 2a(iii)).

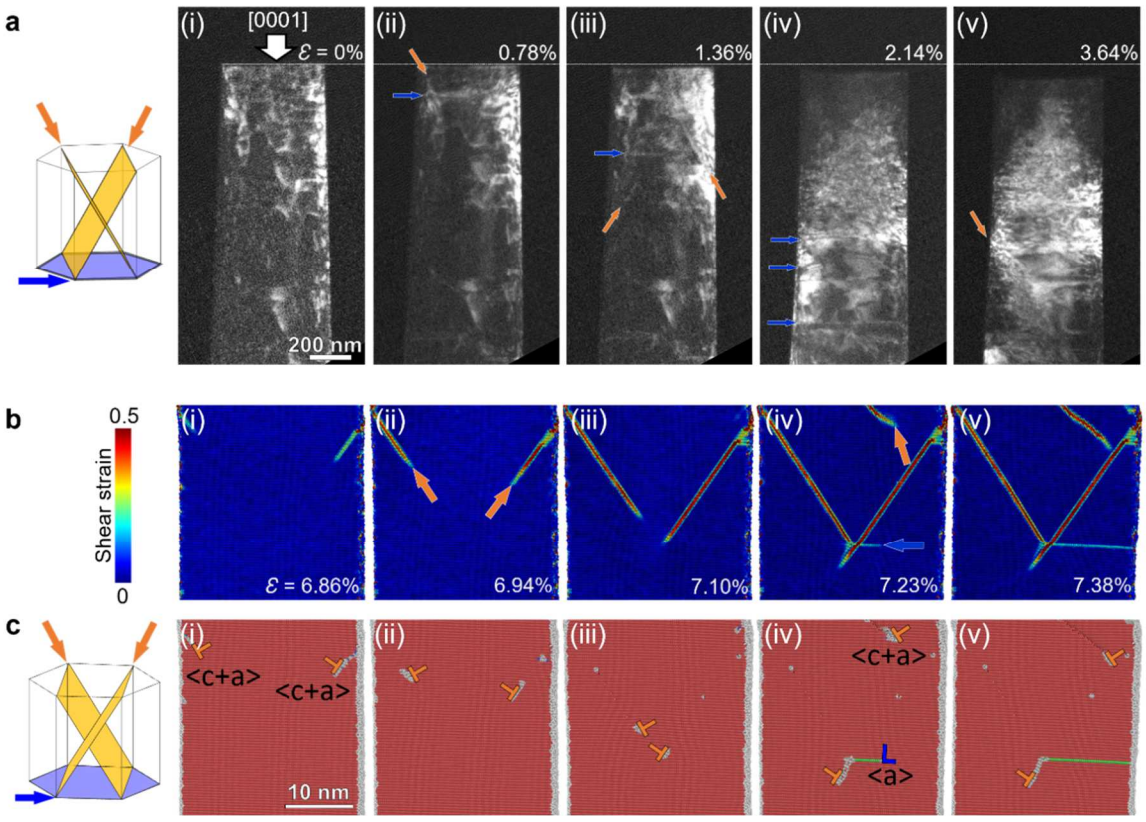

Fig. 2. Evolution of dislocation structure in *c*-axis Mg pillar during compression. (a) Dark-field TEM images of a 500 nm Mg pillar during *in situ* TEM compression test. The inset shows the slip geometry of pyramidal II (orange) and basal (blue) planes for *c*-axis compression. (i) Dark-field TEM image showing pre-existing dislocations before loading. Most dislocations are <*c*+*a*> with straight segments lying along the pyramidal-basal intersection. (ii) Formation of a new dislocation in the initial stage of plastic deformation (0.78% strain). (iii) Multiple slip activated simultaneously on conjugate pyramidal planes. The straight dislocations running along the basal plane are frequently observed together with pyramidal slip of <*c*+*a*> dislocations. (iv) Evolution of dislocation forest by simultaneous activation of multiple dislocation sources, i.e. a dislocation avalanche, at the top of the pillar. The dislocation forest does not propagate downward with further compression. Consecutive

pyramidal slip of a <c+a> dislocation occurring in the lower part of pillar is constrained over a narrow region. (v) Formation of another dislocation forest along the pyramidal plane as a consequence of stress build-up due to the limited pyramidal slip. With further compression, a change in diffraction contrast due to the crystal reorientation is observed as the immobile dislocations in the dislocation forest cannot withstand the stress. (b,c) Atomic configurations of a 30 nm Mg pillar during MD compression test. (i-iii) Nucleation and propagation of <c+a> dislocations on pyramidal II. (iv,v) Activation of basal slip at the junction of two <c+a> dislocations. The atoms in (b) are colored by atomic shear strain. Atoms in (c) are colored according to common neighbor analysis (CNA), where red, green and grey represent atoms in HCP, FCC and other structure, respectively.

With the aim of rationalizing the underlying atomic-scale mechanisms of the dislocation mediated plasticity, MD simulations of compression tests were performed on [0001] and $[2\bar{1}\bar{1}2]$ oriented Mg nanopillars. In line with the experimental observations, a similar orientation-dependent deformation behavior is observed (see Fig. S4). Additionally, as shown in Fig. 2b,c, the MD simulations exhibit similar characteristic defect structures upon *c*-axis compression, e.g., the joint basal and pyramidal II slip traces observed in the *in situ* TEM experiments. Pyramidal II and basal slip systems activated in the compressed [0001]-oriented Mg nanopillar correspond to the motion of full $\langle c+a \rangle$ and partial $\langle a \rangle$ dislocations, respectively. Two full $\langle c+a \rangle$ dislocations nucleate at the free surfaces and propagate on the 'edge-on' conjugated pyramidal II planes (see Fig. 2b,c(i-iii)). A basal stacking fault nucleates at the junction of these two $\langle c+a \rangle$ dislocations (blue arrow in Fig. 2b,c(iv)) and propagates towards the free surfaces. The full $\langle c+a \rangle$ dislocation propagates on the inclined pyramidal II plane, leaving behind a curved slip trace (orange arrow in Fig. 2b(iv)) similar to the experimental observation along the same viewing direction (Fig. 3a).

The $\langle c+a \rangle$ dislocations observed in the *in situ* TEM experiments usually exhibit half-loop and zig-zag configurations. The slip traces of the $\langle c+a \rangle$ dislocations, which make ~58° with respect to the basal plane, are indexed as pyramidal II planes (Fig. 3 and Fig. S5). The plastic strain produced by discrete pyramidal II slip is localized to a narrow region, as the glide of <c+a> dislocations is constrained by the straight sessile segment laid down along the pyramidal-basal interaction. This sessile segment of a $\langle c+a \rangle$ dislocation along the pyramidal-basal intersection is thus attributed to the edge component of $\langle c+a \rangle$ dislocations as the line direction is normal to the Burgers vector (Fig. 3a). The sessile segments neither glide down toward the base of the pillar nor escape through the surface (Fig. 3b). We note that the dislocation multiplication from a single-armed source is rarely seen in the case of the pyramidal slip of $\langle c+a \rangle$ dislocations, which is quite different from the Mg $[2\bar{1}\bar{1}2]$ pillars (Fig. S6, Movie S3) and other FCC pillars with similar sizes[23,26]. This is because the sessile edge component limits bulging or spiraling of the $\langle c+a \rangle$ dislocation line under the resolved shear stress, a prerequisite for source operation. Instead, the sessile edge dislocation exhibits stacking fault contrast on the basal plane, indicating the dissociation into partial dislocations. This then activates pyramidal II slip via dislocation reactions or cross-slip (dotted circle in Fig. 3c). Such pyramidal II slip by individual $\langle c+a \rangle$ dislocations is, however, highly discrete and incapable of ensuring continuous deformation.

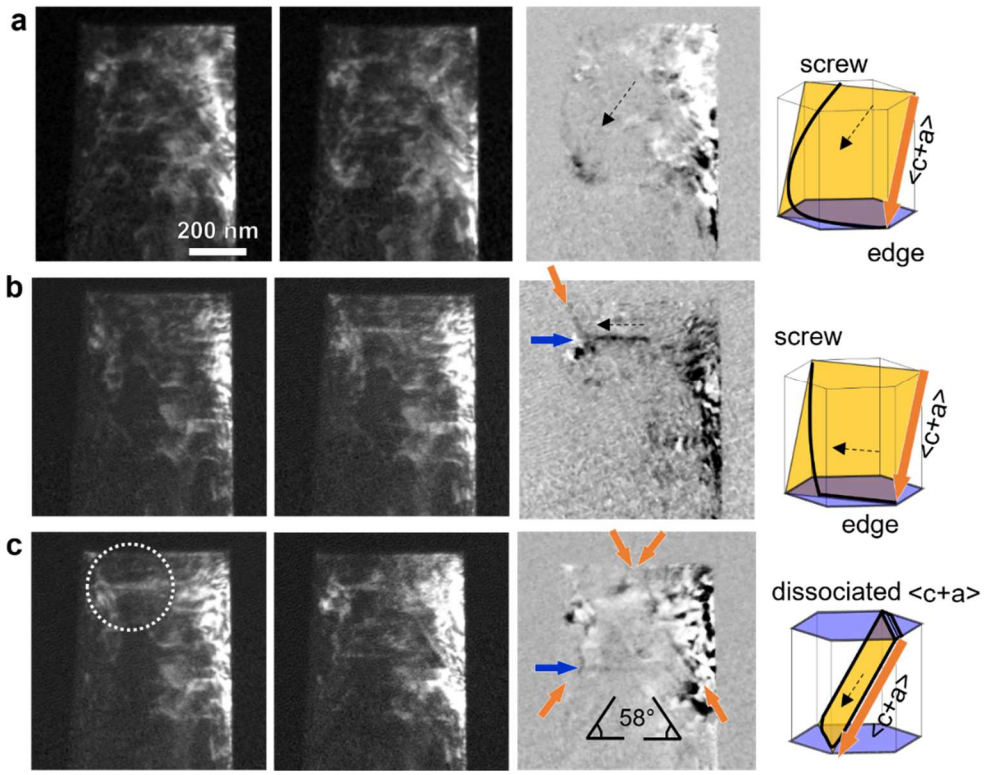

Fig. 3. Discrete pyramidal II slip events of <c+a> dislocations captured by *in situ* TEM. Each set of figures consists of two consecutive dark-field TEM images and their difference (from left to right). (a) Emission of a half-loop. The screw and edge segments of the <c+a> dislocation are indicated. While the screw segment is glissile and escapes through the surface, the edge segment trailing along the pyramidal-basal intersection is sessile. The Burgers vector of the dislocation, <c+a>, is indicated by the orange arrow in the unit cell. (b) Glide of the screw segment trailing the edge segment at the pyramidal-basal intersection. The dislocation line (or slip trace) on pyramidal II and at the pyramidal-basal intersection are marked by orange and blue arrows, respectively. (c) Activation of pyramidal II slip from the sessile <c+a> dislocation dissociated into basal stacking fault. Slip on the conjugate pyramidal II planes is activated from the dissociated <c+a> dislocation (marked by dotted circle). The slip traces, inclined by ~58° with respect to the basal plane, indicate the pyramidal II planes. The dashed line in the schematic drawing delineates the screw segment annihilated through the surface.

2.3 Large strain deformation regime

Intermittent slip events, such as those described above, cannot accommodate large plastic strain at the given strain rate. It causes elastic strain energy to be stored as confirmed by the appearance of bend contours in the TEM diffraction contrast (Fig. 4a, white arrow). This large elastic strain is then released via the simultaneous activation of multiple dislocation sources in the upper half of the pillar, causing dislocation avalanches that form a dislocation forest (Fig. 4a and Fig. 2a(iv)). A high density of sessile dislocations is formed in the dislocation forest by the strongly constrained glide of mobile segments and/or the interactions with other $\langle c+a \rangle$ dislocations. The dislocation forest is thus not effective in relaxing the strain continuously, but induces strain hardening. Plastic deformation is then carried predominantly by intermittent pyramidal slip in the lower half of the pillar (Fig. 4a and Fig. 2a(iv), blue arrow). Upon further loading, for the same reason as previously in the upper half of the pillar, another dislocation avalanche occurs in the region (Fig. 4b and Fig. 2a(v), orange arrow) followed by local bending associated with the accumulation of elastic strain (Fig. 4b). This process is repeated throughout the pillar.

Once the pillar is full of sessile dislocations, further deformation increases the local strain fields and induces slight dislocation rearrangements. The dislocation forest regions undergo severe crystal reorientation as confirmed by the gradual change in diffraction contrast. As confirmed by electron diffraction, the crystal reorientation of the heavily deformed forest region results in the formation of twins. Similar twinning behavior is observed in the simulated compression of [0001]-oriented Mg pillars at high strain level when dislocation density saturates (Fig. 4c-d). Lattice rotation with misorientation angle around 60° is obtained in the severe deformation bands, where shear strain is highly localized (Fig. 4d-e). Two types of compressive twins, $(01\bar{1}1)$ and $(01\bar{1}3)$, are confirmed as the main twinning mechanisms that change crystallographic orientation by 56° and 64°, respectively. The observation of formation of $(01\bar{1}1)$ and $(01\bar{1}3)$ twin bands in the severe plastic deformation regime during the *c*-axis compression correlates well with previous experiments on Mg single crystals[27].

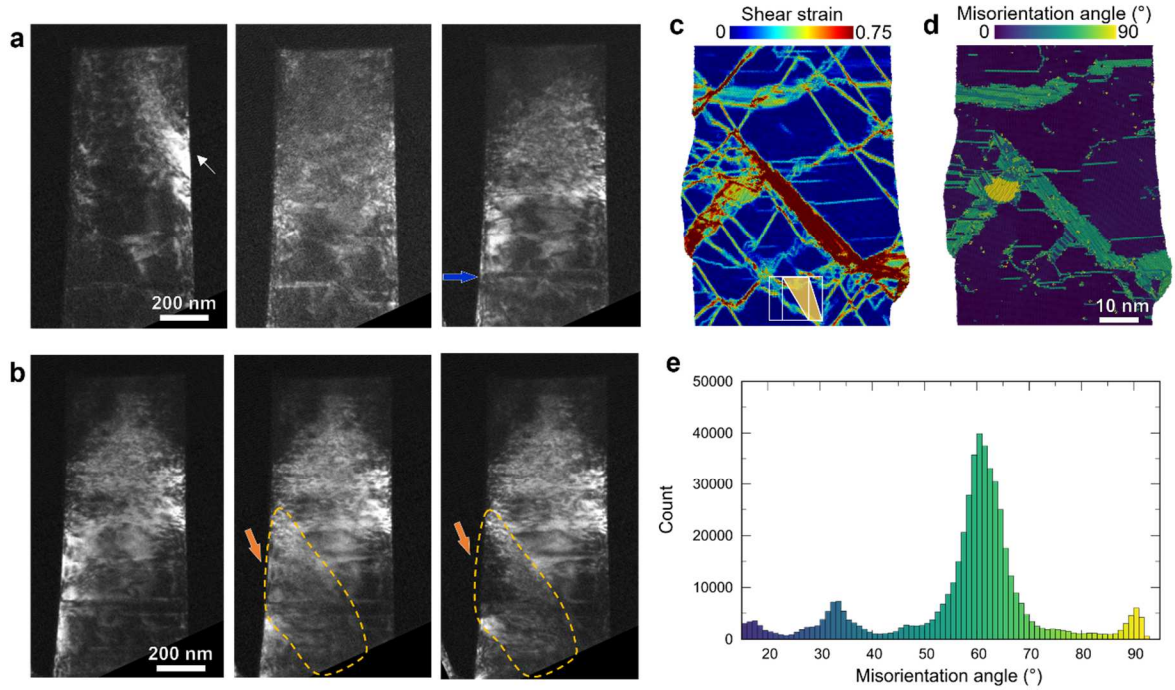

Fig. 4. Dislocation avalanche-like pyramidal II slip – *In situ* TEM and MD simulation. (a) Dark-field TEM images showing the dislocation avalanche in the upper part of pillar followed by discrete pyramidal slip in the lower part. The white arrow indicates the local bending of the pillar caused by the elastic strain before the dislocation avalanche takes place. The subsequent deformation is concentrated in the lower part of the pillar and is carried by discrete pyramidal slip events (blue arrow), while the upper part, full of sessile dislocations, strain-hardens. (b) Dark-field TEM images showing a dislocation avalanche in the lower part (orange arrow). The change in diffraction contrast in the dislocation forest of the upper part indicates crystal reorientation. MD simulation snapshots showing the severe deformation along pyramidal planes by deformation twinning and basal defects colored by (a) atomic shear strain and (d) misorientation angle of the deformed lattice as compared to the undeformed lattice. (e) Lattice reorientation of HCP atoms after the severe deformation of *c*-axis Mg nanopillar in MD compression tests.

2.4 Atomic-scale hardening mechanisms

Surface nucleated $\langle c+a \rangle$ dislocations propagating on six conjugated pyramidal II planes govern the initiation of plasticity in the [0001]-oriented nanopillars under compression. Our MD simulations evidenced that the interactions of these $\langle c+a \rangle$ dislocations and the resulting defect

structures largely contribute to the pronounced strain hardening and are the origin of the limited non-basal plasticity in *c*-axis compression of Mg (Movie S4, Fig. S4). Two hardening mechanisms are identified, involving the formation of different types of basal stacking faults.

Figure 5a shows the interaction mechanism of three $\langle c+a \rangle$ dislocations gliding on different pyramidal II planes and the subsequent formation of basal I_2 stacking faults. The surface nucleated full $\langle c+a \rangle$ dislocations dissociate into pairs of partial dislocations with narrow stacking faults propagating on pyramidal II planes. The interaction of two $\langle c+a \rangle$ dislocations leads to the formation of an $\langle a \rangle$ dislocation (Fig. 5a(ii), solid blue line) on a high-order pyramidal plane, namely $(03\bar{3}4)$. The three $\langle c+a \rangle$ dislocations meet and entangle with each other to form a dislocation junction where multiple partial $\langle a \rangle$ dislocations are formed and propagate on basal planes, leading to the formation of I_2 stacking faults (see Fig. 5a(iii-iv)). The basal I_2 stacking faults then grow until the partial $\langle a \rangle$ dislocations escape at the free surfaces. As shown in Fig. 5a(v-vii), the basal I_2 stacking faults bounded by the dislocation junction and the free surfaces hinder further propagation of pyramidal $\langle c+a \rangle$ and $\langle a \rangle$ dislocations, which is a fundamental requirement of strain hardening.

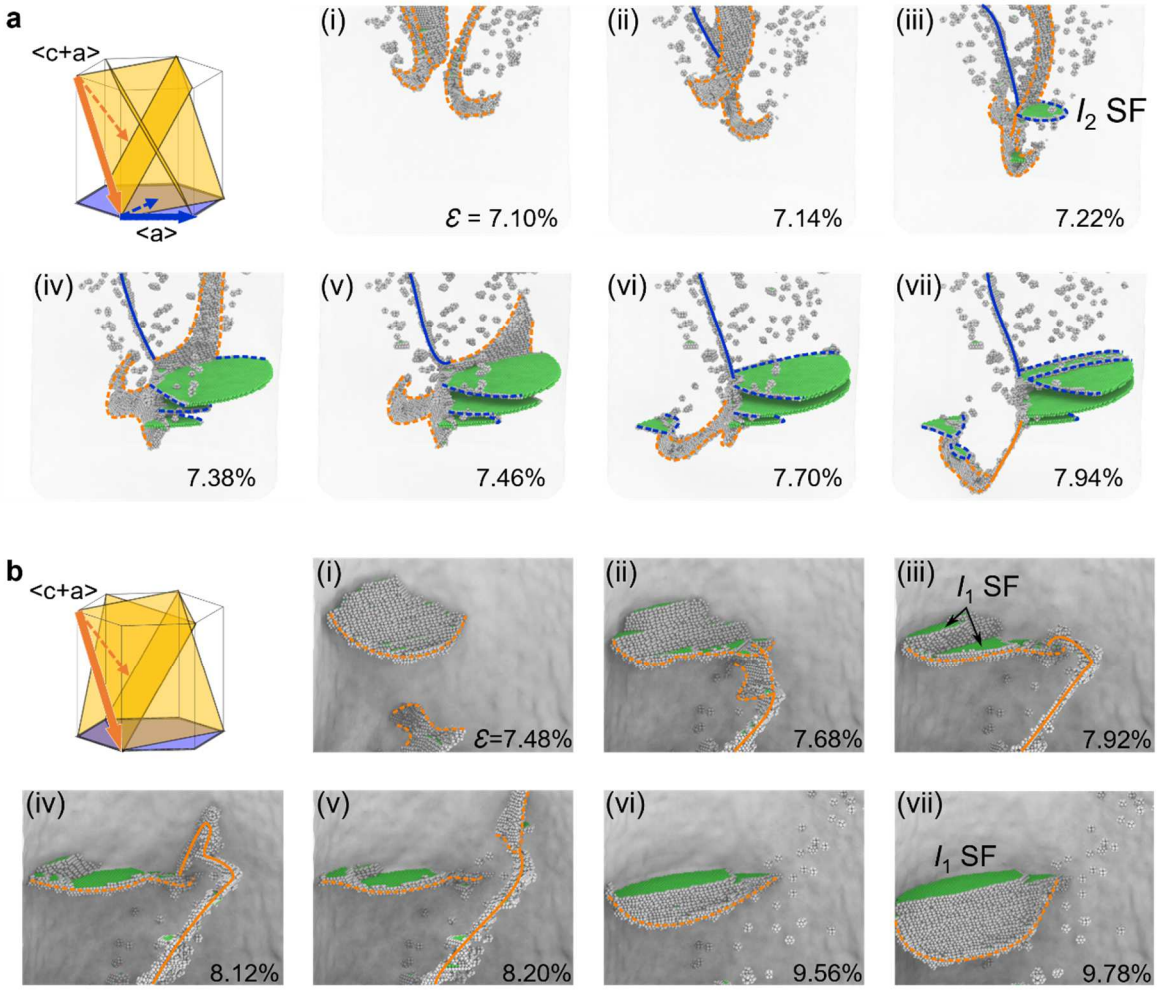

Fig. 5. Interaction mechanism of pyramidal $\langle c+a \rangle$ dislocations and formation of basal stacking faults. (a) Interaction of pyramidal $\langle c+a \rangle$ dislocations and formation of I_2 stacking faults. (b) Transition of partial $\langle c+a \rangle$ dislocation from pyramidal II plane to basal plane and formation of I_1 stacking faults. The inset shows the schematics of slip planes (half-transparent planes), slip on the corresponding planes (dashed lines), and Burgers

vectors (arrows) of activated dislocations. Atoms are colored according to CNA, where green and grey represent atoms in FCC and other structures, respectively. The outer layer atoms and the atoms belonging to the HCP structure are removed. The surface mesh is half-transparent, while dashed and solid lines indicate partial and full dislocation lines, respectively.

Figure 5b illustrates the second hardening mechanism related to the transition of a partial $\langle c+a \rangle$ dislocation from the pyramidal II to the basal plane. The surface nucleated partial $\langle c+a \rangle$ dislocation propagates on a pyramidal II plane and leaves a pyramidal stacking fault behind (see Fig. 5b(i)). A full $\langle c+a \rangle$ dislocation propagating on a conjugated pyramidal II plane interacts with the partial $\langle c+a \rangle$ dislocation (see Fig. 5b(ii-iv)). During this interaction, the partial $\langle c+a \rangle$ dislocation gradually climbs to the basal plane and forms an I_1 stacking fault as shown in Fig. 5b(iii,iv). This basal I_1 stacking fault bounded by the partial $\langle c+a \rangle$ dislocation and free surfaces hinders the propagation of the full $\langle c+a \rangle$ dislocation. While impeded by the basal I_1 stacking fault, cross-slip of the screw segment of the full $\langle c+a \rangle$ dislocation from pyramidal II to I plane occurs (see Fig. 5b(iii,iv)). After disengagement with the I_1 stacking fault, the full $\langle c+a \rangle$ dislocation keeps propagating and escapes at the free surfaces. The partial $\langle c+a \rangle$ dislocation bounding the I_1 stacking fault climbs back to the pyramidal II plane and continues to propagate as shown in Fig. 5b(vi,vii).

In summary, pyramidal and basal I_1 stacking faults act as barriers hindering dislocation motion. Notably, the basal I_1 stacking fault is bounded by free surfaces and a pyramidal stacking fault and, as such, could be annihilated by the glide of a partial $\langle c+a \rangle$ dislocation.

3 Discussion

Our *in situ* TEM mechanical testing in concert with the correlated MD simulations attribute the origins of the pronounced strain hardening of sub-micrometer-size Mg single crystals under *c*-axis compression to the interactions between pyramidal $\langle c+a \rangle$ dislocations and basal defects. This also results in the relatively weak size effect compared to the other orientations.

As reported in previous MD studies[6], the pyramidal-to-basal transitions are thermally activated, stress-dependent and intrinsic to Mg, driven by the reduction in dislocation energy. As observed in recent *in situ* observations[16] and confirmed in this present work, surface nucleated pyramidal $\langle c+a \rangle$ dislocations are glissile under high enough compressive stress along the *c*-axis. However, with increasing dislocation density, the interactions of pyramidal $\langle c+a \rangle$ dislocations trigger the pyramidal-to-basal transitions. This inevitably limits non-basal plasticity and leads to pronounced strain hardening.

Due to the crystallographic symmetry of the *c*-axis loading, there exist six equivalent pyramidal II $\langle c+a \rangle$ slip systems, and abundant surface dislocation sources in the sub-micrometer sample would easily account for the strong strain hardening. However, as observed in our MD simulations, the interactions of pyramidal $\langle c+a \rangle$ dislocations on conjugated slip planes trigger the nucleation of basal dislocations and the propagation of I_2 basal stacking faults. The resolved shear stress on the basal plane due to the interaction-induced local lattice distortion associated with the applied axial compression stress is sufficient to activate the easy basal deformation mode. In addition, the easy-glide pyramidal $\langle c+a \rangle$ dislocations experience a transition to basal I_1 stacking faults under the stress field of other pyramidal $\langle c+a \rangle$ dislocations, which can be attributed to the metastable nature of $\langle c+a \rangle$ dislocations on the pyramidal plane[6–8]. Previously, basal I_1 stacking faults were thought to act as continuous nucleation sources for non-basal dislocations, thereby ductilizing Mg alloys[10–12]. However, in sub-micrometer dimensions, where nucleation is mainly controlled by surface dislocation sources, the contribution of basal

I_1 stacking faults to accommodating the *c*-axis straining of Mg is limited. Rather, we find that basal stacking faults truncate the pyramidal slip systems, thus impeding pyramidal dislocation motion and limiting non-basal plasticity. Thus, to accommodate *c*-axis straining, dislocation avalanches need to take place, which due to the mechanisms outlined above intrinsically induce higher dislocation densities and deformation twins.

In summary, our findings reveal the fundamental mechanisms of the limited non-basal plasticity in small-scale Mg, which is attributed to pyramidal $\langle c+a \rangle$ dislocation interactions instead of previously regarded intrinsic pyramidal-to-basal transitions under *c*-axis straining. A clear understanding of these mechanisms, as provided here for the first time in concert by *in situ* experiments and atomistic modeling, is crucial for materials design strategies to enhance ductility in pure Mg and its alloys.

4 Material and methods

4.1 Sample preparation

A commercially pure Mg single crystal rod was sliced to obtain the [0001] and $[2\bar{1}\bar{1}2]$ crystallographic orientations as surface normal. After specific mechanical polishing, the exact determination of the crystal orientation has been identified by electron backscatter diffraction (EBSD) scans, revealing an angular mismatch of 7 ± 2°. For investigation of the mechanical size effect via mechanical testing in a scanning electron microscope (SEM), cuboid pillars with diameters of 0.5, 1, 2, and 4 µm were fabricated using a focused ion beam (FIB) with a 30 kV Ga^+ ion beam. The pillars had aspect ratios of ~1:3. To investigate the deformation mechanisms of Mg using in-situ TEM experiments, single-crystalline pillars with a diameter of 500 nm were fabricated using FIB. A square shape was used for micron scale pillars for *in situ* SEM experiments to enhance slip plane analysis, while a circular shape was employed for *in-situ* TEM experiments to provide better imaging conditions for dislocations. Annealing at approximately 160 °C was subsequently performed to remove FIB induced defects at the surface of the pillars (Fig. S1). More details are presented in the Supplementary Information.

4.2 In-situ mechanical experiments

Due to the large range of pillar sizes mentioned above, mechanical experiments were performed *in situ* using SEM and TEM, respectively. For testing inside a field emission SEM, two different setups were used. A microindenter system with a maximum applicable force of 300 mN was used for pillars with diameter of 2 µm and 4 µm. For samples with diameter of 1 µm and 0.5 µm, a picoindenter system with a maximum force of 13 mN was used, since a better resolution of force and displacement measurements was necessary. In any case, videos were recorded with one frame per second.

In-situ TEM compression tests were conducted for annealed pillars using a nanoindentation TEM holder in displacement-controlled mode. Real-time movies captured the deformation behavior of the pillars during the compression test at 25 frames per second. More details are presented in the Supplementary Information.

4.3 Molecular dynamics simulations

Compression tests on [0001] and $[2\bar{1}\bar{1}2]$-oriented Mg nanopillars were performed using molecular dynamics (MD) simulations with the software LAMMPS[28]. The interatomic interaction was modeled by a modified embedded-atom method (MEAM) potential for Mg to

favor the pyramidal II $\langle c+a \rangle$ dislocation over pyramidal I[15]. Nanopillars with a circular-shaped cross-section were constructed using Atomsk[29], with diameter of 30 or 60 nm and aspect ratio of 2 or 3. Realistic rough surfaces were created by randomly removing one-third of atoms in the two outermost surface layers, followed by additional annealing and quenching[30,31]. By introducing the surface roughness, the applied stress required to activate dislocations at the free surface is reduced and the distribution of the critical nucleation stresses is broader[32,33]. All pillars were equilibrated for 60 ps at 300 K using the Nosé–Hoover thermostat[34]. Uniaxial compression tests were performed at 300 K under a constant strain rate of 2×10^8 s^{-1} with a time step of 1 fs. The pillars were compressed by virtual indenters at the top and bottom with harmonic spring potentials. The direction of the applied force was parallel to the compression axis. Additionally, compression tests were performed on pillars with semifixed boundary conditions, where the top and bottom atomic layers with thickness greater than two times the potential cutoff were fixed in the direction of compression. To characterize the defect structures, common neighbor analysis[35], polyhedral template matching [36] coordination number, the local von Mises shear strain[37] and the dislocation extraction algorithm (DXA)[38] as implemented in OVITO[39] were used.

Data availability

The raw/processed data required to reproduce these findings cannot be shared at this time as the data also form part of an ongoing study.

Acknowledgements

This work was supported by National Research Foundation of Korea (NRF) grant funded by the Korea government (MSIT) (No. NRF-2020R1A2C2101735), Creative Materials Discovery Program (NRF-2019M3D1A1078296), the Samsung Research Funding & Incubation Center of Samsung Electronics under Project Number SRFC- MA1702-01, and the KENTECH Research Grant (KRG2022-01-019). The TEM work at Korea Institute of Energy Technology (KENTECH) supported by Center for Shared Research Facilities. Z.X. and S.K.K. acknowledge financial support by the Deutsche Forschungsgemeinschaft (DFG) through the projects A02, A05 and C02 of the SFB1394 Structural and Chemical Atomic Complexity – From Defect Phase Diagrams to Material Properties, project ID 409476157. This project has received funding from the European Research Council (ERC) under the European Union's Horizon 2020 research and innovation programme (grant agreement No. 852096 FunBlocks and No. 771146 TOUGHIT). Simulations were performed with computing resources granted by RWTH Aachen University under project (rwth0591), by the EXPLOR center of the Université de Lorraine and by the GENCI-TGCC (Grant 2020-A0080911390).

Author contributions

S.H.O. conceived the project together with D.K. J.J. conducted *in situ* TEM experiments and analysis of TEM data under supervision of S.H.O. M.A. conducted *in situ* SEM microcompression under supervision of D.K. Z.X. conducted MD simulation and data analysis under supervision of J.G. and S.K-K. All authors discussed the data and contributed the writing of manuscript.

Competing interests

The authors declare no competing interests.

References

1. Mordike, B. L. & Ebert, T. Magnesium Properties - applications - potential. *Mater. Sci.*

Eng. A **302**, 37–45 (2001).

2. Kaiser, F. & Kainer, K. U. *Magnesium alloys and technology*. (John Wiley & Sons, 2003).
3. Pollock, T. M. Weight loss with magnesium alloys. *Science (80-.).* **328**, 986–987 (2010).
4. Yoo, M. H. Slip, twinning, and fracture in hexagonal close-packed metals. *Metall. Trans. A* **12**, 409–418 (1981).
5. Geng, J., Chisholm, M. F., Mishra, R. K. & Kumar, K. S. The structure of 〈 c + a 〉 type dislocation loops in magnesium. *Philos. Mag. Lett.* **94**, 377–386 (2014).
6. Wu, Z. & Curtin, W. A. The origins of high hardening and low ductility in magnesium. *Nature* **526**, 62–67 (2015).
7. Wu, Z. & Curtin, W. A. Intrinsic structural transitions of the pyramidal i <c + a> dislocation in magnesium. *Scr. Mater.* **116**, 104–107 (2016).
8. Ahmad, R., Wu, Z., Groh, S. & Curtin, W. A. Pyramidal II to basal transformation of ⟨c + a⟩ edge dislocations in Mg-Y alloys. *Scr. Mater.* **155**, 114–118 (2018).
9. Mises, R. V. Mechanik der plastischen Formänderung von Kristallen. *ZAMM - Zeitschrift für Angew. Math. und Mech.* **8**, 161–185 (1928).
10. Sandlöbes, S., Zaefferer, S., Schestakow, I., Yi, S. & Gonzalez-Martinez, R. On the role of non-basal deformation mechanisms for the ductility of Mg and Mg-Y alloys. *Acta Mater.* **59**, 429–439 (2011).
11. Sandlöbes, S. *et al.* The relation between ductility and stacking fault energies in Mg and Mg-Y alloys. *Acta Mater.* **60**, 3011–3021 (2012).
12. Sandlöbes, S. *et al.* Ductility improvement of Mg alloys by solid solution: Ab initio modeling, synthesis and mechanical properties. *Acta Mater.* **70**, 92–104 (2014).
13. Wu, Z. & Curtin, W. A. Mechanism and energetics of< c+ a> dislocation cross-slip in hcp metals. *Proc. Natl. Acad. Sci.* **113**, 11137–11142 (2016).
14. Wu, Z., Ahmad, R., Yin, B., Sandlöbes, S. & Curtin, W. A. Mechanistic origin and prediction of enhanced ductility in magnesium alloys. *Science (80-.).* **359**, 447–452 (2018).
15. Ahmad, R., Wu, Z. & Curtin, W. A. Analysis of double cross-slip of pyramidal I 〈c+a〉 screw dislocations and implications for ductility in Mg alloys. *Acta Mater.* **183**, 228–241 (2020).
16. Liu, B. Y. *et al.* Large plasticity in magnesium mediated by pyramidal dislocations. *Science (80-.).* **364**, 73–75 (2019).
17. Stohr, P. J. F. & Poirier, J. P. Etude en Microscopie Electronique du Glissement Pyramidal (1122) (1123) dans le Magnesium. *Philos. Mag.* **25**, 1313–1329 (1972).
18. Obara, T., Yoshinga, H. & Morozumi, S. {11$\bar{2}$2}〈1123〉 Slip system in magnesium. *Acta Metall.* **21**, 845–853 (1973).
19. Lilleodden, E. Microcompression study of Mg (0 0 0 1) single crystal. *Scr. Mater.* **62**,

532–535 (2010).

20. Syed, B., Geng, J., Mishra, R. K. & Kumar, K. S. [0 0 0 1] Compression response at room temperature of single-crystal magnesium. *Scr. Mater.* **67**, 700–703 (2012).

21. Fan, H. & El-Awady, J. A. Towards resolving the anonymity of pyramidal slip in magnesium. *Mater. Sci. Eng. A* **644**, 318–324 (2015).

22. Xie, K. Y., Alam, Z., Caffee, A. & Hemker, K. J. Pyramidal i slip in c-axis compressed Mg single crystals. *Scr. Mater.* **112**, 75–78 (2016).

23. Uchic, M. D., Dimiduk, D. M., Florando, J. N. & Nix, W. D. Sample Dimensions Influence Strength and Crystal Plasticity. *Science (80-.).* **305**, 986–989 (2004).

24. Ye, J., Mishra, R. K., Sachdev, A. K. & Minor, A. M. In situ TEM compression testing of Mg and Mg-0.2 wt.% Ce single crystals. *Scr. Mater.* **64**, 292–295 (2011).

25. Korte, S. & Clegg, W. J. Discussion of the dependence of the effect of size on the yield stress in hard materials studied by microcompression of MgO. *Philos. Mag.* **91**, 1150–1162 (2011).

26. Schneider, A. S. *et al.* Influence of bulk pre-straining on the size effect in nickel compression pillars. *Mater. Sci. Eng. A* **559**, 147–158 (2013).

27. Al-Samman, T., Molodov, K. D., Molodov, D. A., Gottstein, G. & Suwas, S. Softening and dynamic recrystallization in magnesium single crystals during c-axis compression. *Acta Mater.* **60**, 537–545 (2012).

28. Thompson, A. P. *et al.* LAMMPS - a flexible simulation tool for particle-based materials modeling at the atomic, meso, and continuum scales. *Comput. Phys. Commun.* **271**, 108171 (2022).

29. Hirel, P. Atomsk: A tool for manipulating and converting atomic data files. *Comput. Phys. Commun.* **197**, 212–219 (2015).

30. Bitzek, E., Koskinen, P., Gahler, F., Moseler, M. & Gumbsch, P. Structural relaxation made simple. *Phys. Rev. Lett.* **97**, 170201 (2006).

31. Guénolé, J. *et al.* Assessment and optimization of the fast inertial relaxation engine (FIRE) for energy minimization in atomistic simulations and its implementation in LAMMPS. *Comput. Mater. Sci.* **175**, 109584 (2020).

32. Xie, Z. *et al.* Origins of strengthening and failure in twinned Au nanowires: Insights from in−situ experiments and atomistic simulations. *Acta Mater.* **187**, 166–175 (2020).

33. Schrenker, N. J. *et al.* Microscopic Deformation Modes and Impact of Network Anisotropy on the Mechanical and Electrical Performance of Five-fold Twinned Silver Nanowire Electrodes. *ACS Nano* **15**, 362–376 (2021).

34. Hoover, W. G. Canonical dynamics: Equilibrium phase-space distributions. *Phys. Rev. A* **31**, 1695–1697 (1985).

35. Honeycutt, J. D. & Andersen, H. C. Molecular dynamics study of melting and freezing of small Lennard-Jones clusters. *J. Phys. Chem.* **91**, 4950–4963 (1987).

36. Larsen, P. M., Schmidt, Sø. & SchiØtz, J. Robust structural identification via polyhedral

template matching. *Model. Simul. Mater. Sci. Eng.* **24**, (2016).

37. Shimizu, F., Ogata, S. & Li, J. Theory of shear banding in metallic glasses and molecular dynamics calculations. *Mater. Trans.* **48**, 2923–2927 (2007).

38. Stukowski, A., Bulatov, V. V. & Arsenlis, A. Automated identification and indexing of dislocations in crystal interfaces. *Model. Simul. Mater. Sci. Eng.* **20**, (2012).

39. Stukowski, A. Visualization and analysis of atomistic simulation data with OVITO-the Open Visualization Tool. *Model. Simul. Mater. Sci. Eng.* **18**, 15012 (2010).

Supplementary Files

This is a list of supplementary files associated with this preprint. Click to download.

- MovieS1.avi
- MovieS2.mp4
- MovieS3.mp4
- MovisS4.mp4
- SIManuscriptMgpillarsMaterialsTodayfinalSHO.pdf